Simultaneous Determination of Non-Uniform Soot Temperature and Volume Fraction from Flame Images

Chengyong Liu[1, a], Liang Cheng[1, b], Yipeng Sun[1, *], Weijie Yan[2, c], Kuangyu Li[2, d]

[1]North China Electric Power Research Institute CO., Ltd, Beijing, China

[2]School of Low-Carbon Energy and Power Engineering, China University of Mining and Technology Xuzhou, China

* Corresponding Author Email: syp1103@qq.com, [a]liuchengyong@foxmail.com, [b]chengliang79@126.com, [c]yanweijie@cumt.edu.cn, [d]likuangyu@cumt.edu.cn

Abstract. This paper presents a method to invert the two-dimensional distribution of temperature and volume fraction of soot particles from flame images. The temperature field and particle volume concentration field of the non-uniform soot flame are simultaneously reconstructed using the wide response spectrum of the color CCD camera without adding monochromatic filters. The influences of the number of cameras, error of cameras position angle, measurement noise and different reconstruction algorithms on the measurement accuracy, are analyzed. The numerical simulation results demonstrate that the error of cameras position angle plays a crucial role in the reconstruction accuracy. In addition, increasing the number of cameras can improve the reconstruction results accuracy. Compared with the least squares algorithm, the Tikhonov regularization algorithm has a stronger anti-noise ability, which can resist 39 dB of noise. The conclusions obtained in this paper are helpful to guide the following experimental studies.

Keywords: asymmetric flame, images processing, soot temperature, soot volume fraction, tomographic reconstruction.

1. Introduction

Flame temperature is an important combustion parameter [1, 2]. The accurate temperature is of great significance to improve the combustion efficiency and reduce the pollutant emissions [3]. The thermocouple temperature measurement is one of the most common temperature measurement methods, which has the advantages of simple operation and reliable results. However, it is a contact measurement method, and it is easy to interfere with the measured flame flow filed, thereby affecting the temperature field distribution of the flame [4, 5]. The non-contact measurement will not interfere with the measured flame flow field, which has certain advantages in flame temperature measurement. The laser spectroscopy is one of the non-contact temperature measurement methods, including laser interference holography [6-8], tunable semiconductor laser absorption spectroscopy (TDLAS) technology [9-12] and scattering (LRS) technology [13-16]. In recent years, the measurement of the temperature fields of the flame section has been performed by combining the TDLAS and CT technologies [11, 17, 18]. The laser spectral temperature measurement technology has the advantages of high measurement accuracy and large measurement range. However, the temperature measurement process requires the lasers. In addition, the corresponding optical paths are arranged, and the operation process has a certain complexity. It is challenged to use laser spectroscopy for temperature measurement in some high-vibration and high-dust industrial environments[19-21].

The temperature measurement technology based on flame spontaneous radiation information is another type of non-contact passive temperature measurement methods, which does not require a laser light source[22]. During the fuel combustion process, a large amount of heat is released due to the chemical reaction, which is externally manifested as a thermal radiation spectrum. When measuring the flame temperature based on the flame excitation radiation information, it is necessary to use a sensor to collect the thermal radiation information. As the most common industrial camera, the CCD camera is widely used in temperature measurement due to its advantages [23-26]. This method has the advantages of not affecting the measured flame flow field and without an external light source. The entire flame flow field information can be collected by a CCD camera, and several algorithms can be used to reconstruct the flame flow field parameters[27, 28].

The algorithm used to reconstruct the flame flow field consists in inverting the radiation source term of the flame flow field from the boundary radiation intensity collected by the CCD camera. The process of inversion need a high computational load and it is time-consuming. In addition, it is prone to errors due to the considered ill-posed problem. Now, it is mainly divided into two categories: optimization algorithms [29-32] and regularization algorithms [33-36]. Liu et al. [29] transformed the inversion problem into an optimization problem. The conjugate gradient method was used to obtain the boundary radiation intensity with the smallest error from the experimental data. Wang et al. [30] transformed the inversion problem into an ill-conditioned matrix. The least squares QR decomposition algorithm was used to solve the optimal radiation source term, and the parameters of the flame flow field from the optimal radiation source term were obtained. The least squares QR decomposition algorithm is more advantageous in terms of the processing numerical properties. The optimization algorithm is well developed, and is widely used to solve such inversion problems. However, the optimization algorithm is an iterative algorithm which requires to set the suitable convergence range. An inappropriate convergence range will lead to large errors, long calculation time. Zhou et al.[37] proposed an improved Tikhonov regularization algorithm for the reconstruction of three-dimensional temperature field. The obtained error of the experimental results is almost 5%. Wei et al. [38] improved the overall accuracy of reconstruction using the Tikhonov regularization algorithm. Xie et al. [39] used both the Tikhonov regularization algorithm and the truncated singular value algorithm to reconstruct the flame in the furnace. The experimental results demonstrate that the former takes less time, the reconstruction error is small, and the maximum temperature is more accurate. Previous studies have shown that the Tikhonov regularization algorithm can accurately reproduce the distribution of different parameters of the flame flow field, and has a great potential.

In previous studies, the wavelengths of the three channels of the camera are often approximated by the monochromatic wavelength, in order to calculate the radiation intensity [40-44]. However, the spectral response of the R, G and B bands of the color CCD camera is relatively wide, and can not be simply approximated by the monochromatic wavelength. Yan et al. [45] considered the broad spectrum of the color CCD camera to invert axisymmetric flames. The experimental results show that this method is efficient and reliable.

Based on the previous studies, this paper uses a color CCD camera to collect flame images, and reconstructs the two-dimensional temperature field and radiation characteristics of the flame by the Tikhonov regularization algorithm, and per-forms the verification in the numerical simulation of the bimodal flame. Three steps are divided: establishing a numerical simulation of a double-peak flame, calculating the image intensity collected by the camera according to the spectral band model, and using the Rayleigh approximation formula to calculate the spectral absorption coefficient. The calculated image intensity is used to reconstruct the temperature field distribution of the flame section by the Tikhonov regularization algorithm. Finally, the reconstruction results are compared with those obtained using the LSQR algorithm.

2. Reconstruction principle

2.1. Radiation imaging models

The tomographic reconstruction of asymmetric flames usually requires multiple angles to provide a complete distribution information of the flame. If images of flames are used for reconstruction, multiple cameras are required. To this end, this paper proposes a flame cross-section radiation parameter reconstruction system, which is specially designed to perform the multi-camera tomographic reconstruction of the flame, as shown in Figure 1. Multiple cameras are placed at the same angle α and same distance from the flame axis. The flame images are then simultaneously collected. The pixel intensity of the flame image is processed in order to obtain the radiation source term distribution of the flame cross-section. The cross-section temperature distribution of the flame is then calculated by colorimetry, as described in the next section.

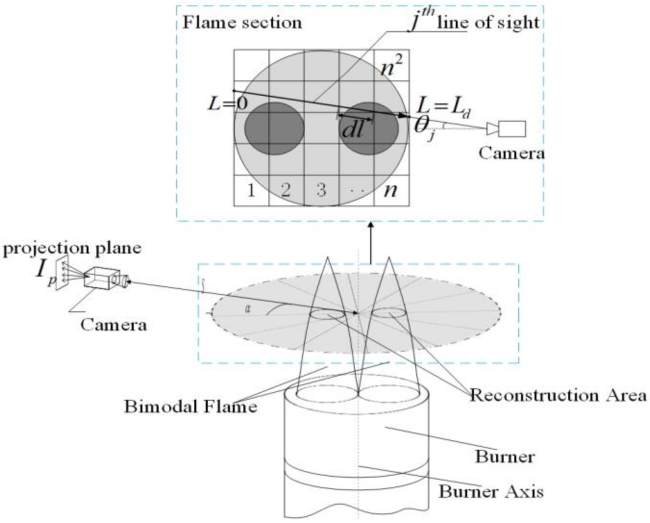

Figure 1. Multi-camera tomographic reconstruction system.

2.2. Direct problem

For hydrocarbon fuel combustion flames, the radiation of CO_2 and H_2O in the visible light band is negligible, while the ra-diation of the flame in the visible light band is mainly generated by soot at high temperature [46]. In general, the flame radiation intensity on the flame section is described by the Radiation Transfer Equation (RTE)[40], in which only the effects of flame scattering and self-absorption are considered. In this paper, the following assumptions are made: (a) only the soot radiation in the visible light band is considered; (b) the effects of scattering and self-absorption of the flame are ignored; (c) the effect of back-ground light radiation is ignored.

According to these assumptions, the projection of the radiation source term of the flame section along the projection path received by the camera, can be expressed as:

$$I_\lambda = \int_0^{L_d} \kappa(L,\lambda) I_b\,(L,\lambda) dl \tag{1}$$

Where λ is the wavelength , L represents the projected path length, $I_b(L,\lambda)$ denotes the blackbody radiation intensity of soot particles, and $\kappa(L,\lambda)$ is the local spectral absorption coefficient which is proportional to the soot volume fraction, and calculated by the Rayleigh limit of Mie theory as:

$$\kappa_a = \frac{6\pi E(m) f_v}{\lambda} \tag{2}$$

where $E(m)$ is the soot optical constant and m is the gradient index function with real and imaginary parts.

Note that $E(m)$ is related to the physical properties of soot. In this study, the most widely used function model in the literature is considered. More precisely, $E(m) = 0.26, m = 1.57 - 0.56i$[47].

According to Plank's law, the radiation intensity of soot particles can be expressed as:

$$I_b(L,\lambda) = \frac{C_1 \lambda^{-5}}{e^{\frac{C_2}{\lambda T(L,\lambda)}} - 1} \frac{1}{\pi} \tag{3}$$

where $T(L,\lambda)$ represents the temperature, and C_1, C_2 are the first and second radiation constants, respectively.

In previous studies, when computing the radiation intensity of soot particles, the R, G and B data of the pixels of the flame picture collected by color CCD camera are usually assumed proportional to the approximately monochromatic radiative intensities in wavelength of red, green and blue [40-43]. However, due to the wide spectral response spectrum of the R, G and B channels of the color camera, it cannot be simply approximated by the monochromatic radiation intensity. Assuming that the relative spectral response efficiencies of the R, G and B channels of the CCD camera are expressed as: $\eta_R(\lambda), \eta_G(\lambda), \eta_B(\lambda)$, the projection received by the camera can be expressed as:

$$I_\lambda = \int_0^{L_d} \int_\lambda \eta_k(\lambda)\kappa(L,\lambda)I_b(L,\lambda)d\lambda dl$$
$$k = R, G, B \tag{4}$$

As shown in Figure 1, the flame cross section and camera beam are respectively discretized into n^2unit grids and $p$imaging sight lines, where the flame radiation parameters in the unit grids are uniform. Therefore, equation (3) can be written in a discrete form:

$$I_\lambda(j) = \sum_{i=1}^{n^2} \int_\lambda \eta_k(\lambda)\kappa(i,\lambda)I_b(i,\lambda)d\lambda \Delta L_{j,i}$$
$$I_\lambda(j) = \sum_{i=1}^{n^2} I(i,\lambda)\Delta L_{j,i} \tag{5}$$
$$j=1, \dots, p$$

where $I_b(i,\lambda)$ is the radiation source term of the cell grid number$i$, $\eta_k(\lambda)$ represents the relative spectral response efficiencies, $\kappa(i,\lambda)$ denotes the local spectral absorption coefficient of grid number$j$, and$\Delta L_{j,i}$is the distance traveled by the imaging sight line number$j$within the grid number i.

Equation (5) is then written in matrix form:

$$\boldsymbol{I}_\lambda = \Delta\boldsymbol{S} \cdot \boldsymbol{I} \tag{6}$$

where $\Delta\boldsymbol{S} \in R^{P\times n^2}$,$\boldsymbol{I}_\lambda \in R^pand\boldsymbol{I} \in R^{n^2}$

It can be seen from Figure 1 that each imaging line of sight will only pass through few cell grids. Therefore, matrix $\Delta\boldsymbol{S}$ is a large sparse matrix, and an ill-posed matrix solution algorithm is required to invert reasonable results. For the inversion algorithm of large sparse matrices, the commonly used methods are the Tikhonov regularization algorithm and the least squares (LSQR) algorithm based on QR decomposition. In this paper, these two algorithms are used to simultaneously reconstruct the radiation parameters of the flame section, and the influence of different measurement errors on the accuracy of the two reconstruction algorithms is evaluated.

2.3. Inverse problem

The Tikhonov regularization algorithm [35] can transform the solving of equation (6) to the solving of the minimum of the following expression:

$$R(\boldsymbol{I},\alpha) = \|\boldsymbol{I}_\lambda - \boldsymbol{\Delta S} \cdot \boldsymbol{I}\|^2 + \alpha\|\boldsymbol{D} \cdot \boldsymbol{I}\| \tag{7}$$

where $\boldsymbol{D}$ is a regularized matrix whose diagonal elements are all 1.0, and the sum of all the elements in each row is 0[34].

An approximate solution for the regularization coefficient α is given by [43]:

$$\alpha(\boldsymbol{I}_\lambda) \approx \frac{2\|\boldsymbol{I}_\lambda - \boldsymbol{\Delta S} \cdot \boldsymbol{I}(0)\|^2}{\|\boldsymbol{D} \cdot \boldsymbol{I}(0)\|^2} \tag{8}$$

where $\boldsymbol{I}(0)$ is the least squares solution of equation (6).

The optimal solution of equation (6) is then expressed as:

$$\boldsymbol{I} = (\boldsymbol{\Delta S}^T \boldsymbol{\Delta S} + \alpha \boldsymbol{D}^T \boldsymbol{D})^{-1} \boldsymbol{\Delta S}^T \boldsymbol{I} \tag{9}$$

After solving the radiation source term distribution of the flame section, the temperature distribution can be solved using the two-color method:

$$\frac{I_r}{I_g} = \frac{\int_\lambda \eta_r(\lambda)\kappa_r(\lambda)I_{b,r}d\lambda}{\int_\lambda \eta_g(\lambda)\kappa_g(\lambda)I_{b,g}d\lambda} \tag{10}$$

where I_r and I_r are the source term distributions of radiation for the R and G channels, respectively.

Since equation (10) comprises the integral of wavelength λ, it cannot be simply solved. Therefor this paper develops equation (11) about temperature T and uses the Newton iteration method to solve the temperature distribution:

$$F(T) = I_r \int_\lambda \eta_g(\lambda) \frac{C_1\lambda^{-6}}{e^{\frac{C_2}{\lambda T}}} d\lambda - I_g \int_\lambda \eta_r(\lambda) \frac{C_1\lambda^{-6}}{e^{\frac{C_2}{\lambda T}}} d\lambda \quad (11)$$

After the temperature distribution is solved, the soot concentration distribution can be reversely solved by bringing the temperature distribution into equation (3). The overall calculation process is presented in figure 2.

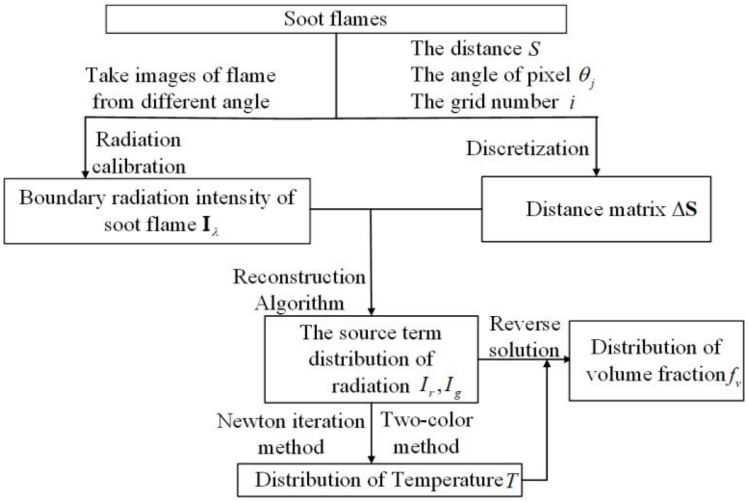

Figure 2. The overall calculation process

3. Simulated object

The impacts of different errors on the reconstruction accuracy of the two algorithms are compared using a numerical simulation. The asymmetric temperature and soot concentration distributions are expressed in equation (12). In this system, the cam-eras are assumed to have a field of view of 11.4 degrees and the distance is 169 mm. The common area that the cameras can capture is a circle with a diameter of 33.78 mm in the central area. Therefore, the flame cross section is divided into 1600 sub-units and each sub-units is a square with a side length of 0.6 mm in space.

$$T(x,y) = 1800e^{-\left(\frac{x^2+y^2}{2500}\right)}$$

$$f_v(x,y) = \frac{1}{T(x,y)} \quad (12)$$

where $-19 \le x \le 20$,$-19 \le y \le 20$, $T(x,y)$ and $f_v(x,y)$ are respectively the temperature and soot concentration distributions, as shown in Figure 3.

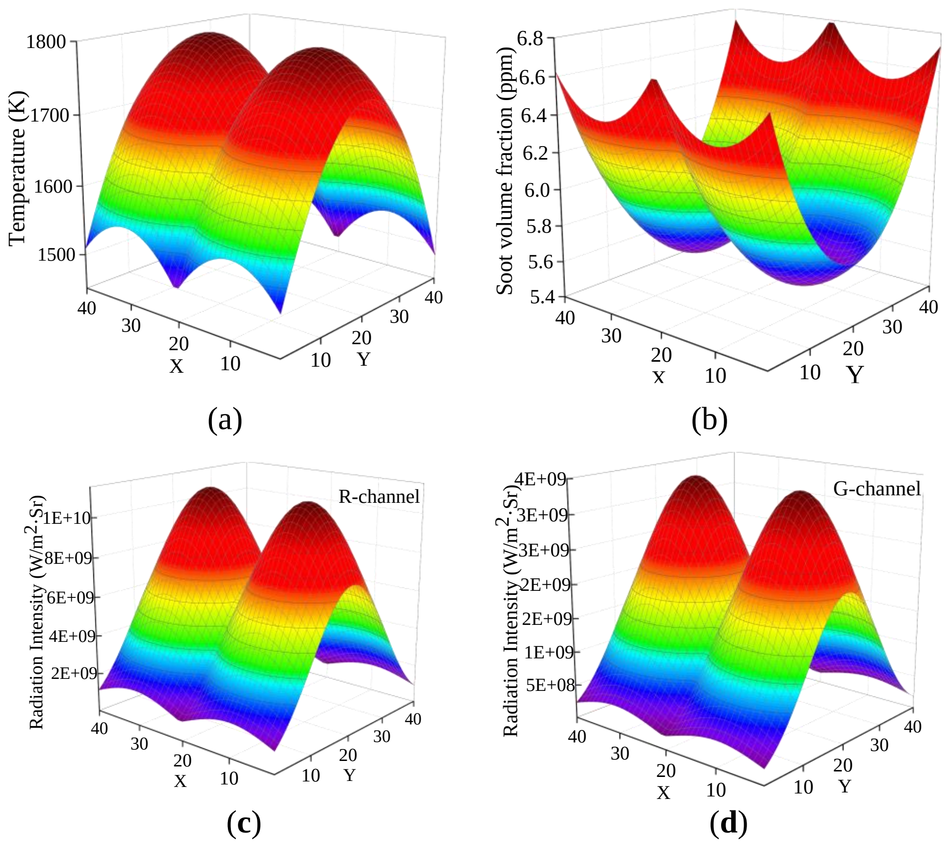

Figure 3. Cross section of the assumed twin peaks flame for numerical simulation: (a) Temperature distribution of the flame; (b) Soot concentration distribution of the flame; (c) Radiation source term distribution of channel R; (d) Radiation source term distribution of channel G.

In this paper, the Gaussian function is used to approximate the relative spectral response efficiency, function of the simulated CCD camera:

$$\eta_i(\lambda) = C_i\, exp\left[-\frac{(\lambda-a_i)^2}{4000}\right] \tag{13}$$

$$i = R, G$$

where C_i is the maximum relative spectral response efficiency and a_i is the central wavelength.

It is assumed that $C_G = 1$, $C_R = 0.8$,$a_R = 600$ and $a_G = 500$. The relative spectral response efficiency curves of the R and G channels are shown in Figure 4.

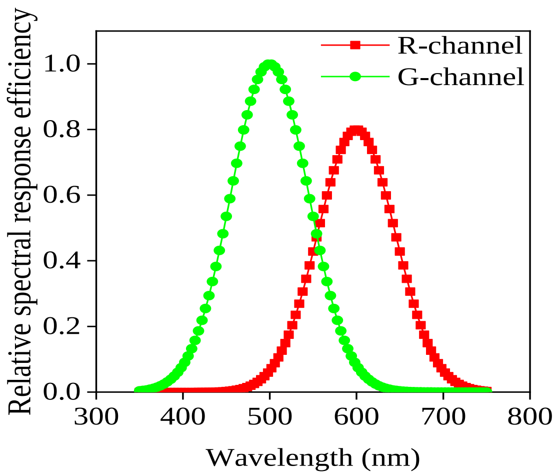

Figure 4. Relative spectral response efficiency functions of the R and G channels, simulated by a Gaussian function.

For the actual flame, only the flame image collected by the CCD camera is required as the projection data in order to invert the radiation parameters of the flame section. However, for the numerical simulation, mathematical methods should be used to calculate the theoretical radiation intensity collected by CCD cameras at different angles. In this paper, in the multi-camera reconstruction system of flame section radiation parameters construction, three cases of camera placement interval angle exist: $\alpha = 30°$, $\alpha = 60°$and $\alpha = 90°$corresponding to 12, 6 and 4 cameras, respectively. The theoretical radiation intensity distribution collected by the CCD camera is shown in Figure 5.

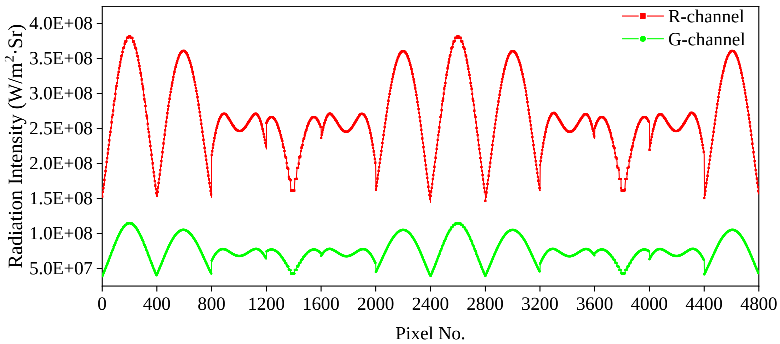

Figure 5. Theoretical radiation intensity of the R and G channels collected by 12 CCD cameras with 400 pixels per camera (up to 4800 pixels).

In this paper, the root mean square error (RMS) is used to test the accuracy of the reconstructed field with the known original intensity field:

$$E = 100\frac{\sqrt{\frac{1}{N}\sum(f(x,y)-f(x,y)\prime)^2}}{f_{max}} \tag{14}$$

where $f(x,y)$ is the reconstructed field, $f(x,y)'$ represents the original intensity field, f_{max} denotes the maximum value of the original intensity fields, and N is the number of cell grids equal to 1600 as previously mentioned.

4. Results and discussion

4.1. Influence of the number of cameras

As previously mentioned, three cases for the number of cameras exist: four cameras separated by 90°, six cameras sepa-rated by 60° and twelve cameras separated by 30°. The root mean square error of the reconstruction results for the two algorithms with different numbers of cameras, is shown in Figure 6.

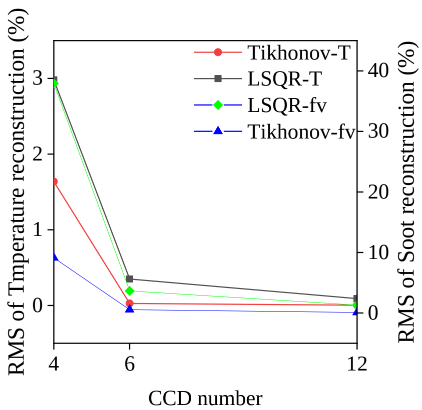

Figure 6. The RMS of the two algorithms for the reconstruction temperature and soot concentration variation with the number of cameras.

When the number of CCD cameras increases, the reconstruction effect of the two algorithms is better. Due to the fact that the two algorithms are equations for large sparse matrices, as the number of CCD cameras increases, more projection data can be provided, and therefore the inversion results are better. Since the horizontal field of view of the camera is smaller than the separation angle of the cameras, the line of sight passing between the cameras is less, which results in more prone to distortion at the boundary. The reconstruction of the soot concentration distribution is more prone to distortion than the reconstruction of the temperature distribution. The regularization algorithm outperforms the least squares algorithm, for both temperature and soot concentration reconstructions. When the number of CCD cameras is more than six, the two algorithms can reconstruct better temperature distribution. However, for the soot concentration reconstruction, only the regularization algorithm can obtain better results.

It can be observed from Figure 6 that, as the camera interval angle decreases and the number of cameras increases, the reconstruction accuracy of the two algorithms is greatly improved. The temperature reconstruction error of the regularization algorithm decreases from 1.63% for four cameras to 0.0027% for twelve cameras. In addition, the reconstruction effect of soot concentration is more easily affected by the number of CCD cameras. The soot concentration reconstruction error of the four-camera regularization algorithm reaches 9.11%, while the error of the LSQR algorithm also reaches 39.8%. When the number of CCD cameras increases to twelve, the error also decreases to the same level as the temperature reconstruction. Therefore, the error of the regularization algorithm is 0.0885%, and that of the LSQR algorithm is 1.30%.

4.2. Effect of measurement noise

When a camera is used to collect flame images, it is inevitable that the external light sources, attenuation of flame light and other factors will affect the collected flame images, which affects the reconstruction accuracy. Two algorithms can accurately reconstruct the distribution of temperature and soot concentration. Therefore, in the case of limited noise, the two algorithms should also be able to more accurately reconstruct the radiation parameters of the flame section. In order to analyze the anti-noise ability of the two algorithms, a random noise (cf. equation (15)) is added to the previously described theoretical radiation intensity. In order to avoid the reconstruction error caused by the lack of flame information collected by the camera and the two-color method, the influence of noise on the two algorithms is analyzed using the reconstruction results of the radiation source terms of twelve cameras.

$$I'_\lambda = I_\lambda \left(1 + \frac{R_{12}-6}{\sigma}\right) \tag{15}$$

where I'_λ and I_λ respectively represent the theoretical radiation intensity after adding noise and without adding noise, and R_{12} is the sum of 12 random numbers between 0 and 1, representing different noise levels.

$$SNR = 20\, lg\left(\frac{I'_\lambda}{I'_\lambda - I_\lambda}\right) \tag{16}$$

In this paper, the signal-to-noise ratio (SNR) is used to evaluate the noise intensity. The SNR is calculated (in dB) using equation (16). In the calculation process, four different noise levels are considered: $\sigma = 50, \sigma = 800, \sigma = 900$ and $\sigma = 2200$. The corresponding SNRs are: 39dB, 63dB, 65dB and 72dB, respectively. The reconstruction error results are shown in Figure 7.

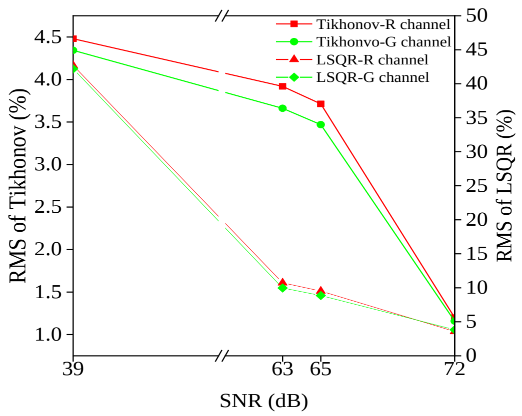

Figure 7. Influence of different intensity noises on the reconstruction accuracy of the two algorithms.

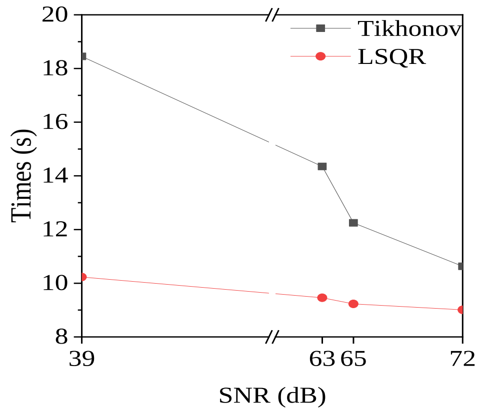

Figure 8. The time taken by the two algorithms for different intensity noises.

It can be seen from Figure 7 that, as the noise level decreases, the reconstruction effect of the two algorithms gradually becomes better. A comparison of the two algorithms shows that the regularization algorithm introduces the regularization matrix $\boldsymbol{D}$ and the regularization coefficient α based on the LSQR algorithm, and obtains the final result by the inversion of the ill-posed matrix. Therefore, the regularization algorithm has a stronger anti-noise ability than the LSQR algorithm. Although the SNR reaches 39dB, the reconstruction error of the regularization algorithm is only almost 4%. In addition, the regularization algorithm can still accurately reconstruct the radiation source term distribution. The anti-noise ability of the LSQR algorithm is far less than that of the regularization algorithm. Only when the SNR is reduced to 63dB, the LSQR algorithm can have a reconstruction error of almost 10%. However, it is still higher than the regularization algorithm by almost 4%.

Moreover, the time consumed by the reconstruction process is also important to the evaluation of the algorithm, Figure 8 represents the time consumed by the two algorithms, under different noise levels. It can be seen that the regularization algorithm takes slightly longer time than the LSQR algorithm. This is due to the fact that the LSQR algorithm is the basis of the regularization algorithm, both of which require to iterate the matrix, and the regularization algorithm also requires to further regularize the iterative results of the LSQR algorithm, which results in a longer time needed by the regularization algorithm. In general, as the number of elements of the coefficient matrix increases, the iteration time required by the LSQR algorithm sharply increases, which results in an increase in the algorithm time. However, increasing the number of cells in the reconstructed source term will increase the reconstruction accuracy. Therefore, it is necessary to make a trade-off between the reconstruction time and reconstruction accuracy, in order to achieve an efficient balance between them.

4.3. Error of camera separation angle

As previously mentioned, the camera separation angles (30°, 60° and 90°) are the same. However, in the actual experiment, the angle between the cameras will inevitably have an angle deviation due to experimental equipment, reading errors and other reasons. In order to analyze the influence of the angle deviation on the reconstruction accuracy of the two algorithms, different degrees of angle error are added to the acquisition angles of the twelve cameras, and the radiation source term is reconstructed accordingly. The obtained results are shown in Figure 9.

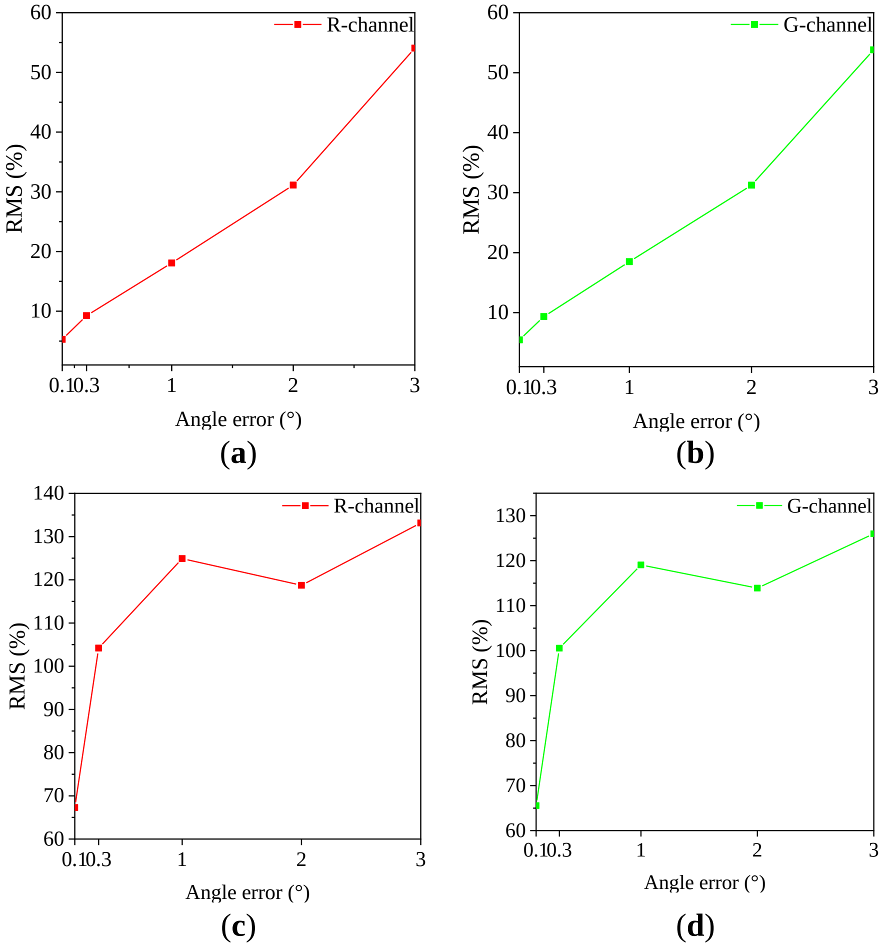

Figure 9. Influence of different interval angle errors on the reconstruction accuracy of the two algorithms. Influence on the regularization algorithm of channel R (a) and channel G (b), influence on the LSQR algorithm of channel R (c) and channel G (d).

It can be seen from Figure 9 that four angular errors of 0.1°, 0.3°, 1° and 3° are added to the acquisition angle. The radiation source terms of the R and G channel reconstruction of the two algorithms are highly affected by the interval angle error. In addition, the RMS rapidly increases with the increase of the error angle. When the angle error is 2°, the RMS of the regularization algorithm exceeds 30%, and the reconstruction results at this time can no longer be used to reconstruct the radiation parameters of the flame section. The impact of the LSQR algorithm is far greater than that of the regularization algorithm. More precisely, when the angle error is 0.1°, the reconstruction error of the LSQR algorithm exceeds 60%. It can be deduced from this analysis that the camera acquisition angle is highly important for the two algorithms, and it is the basis for determining whether the inversion can be achieved. By analyzing the generation principle of the theoretical images, the reason why the angle error has a high influence can be determined. In fact, the flame image is a "cumulative effect" formed by a specific radiation source item, a specific acquisition angle, a specific line if sight and a specific grid. The deviation of the angle when collecting the flame image will cause the flame images provided by multiple cameras to be contradictory, which leads to inversion errors. In contrast to the effects of the number of cameras and noise on the previously detailed two algorithms, the camera acquisition angle affects the inversion process, while its impact on the two algorithms is extremely significant.

5. Conclusions

This paper proposes a method to simultaneously reconstruct the two-dimensional temperature field and soot particle volume concentration for non-uniform soot flame, using the wide response spectrum of a color CCD camera. It then evaluates the influence of the number of cameras, camera interval angle error and noise on the Tikhonov regularization algorithm and LSQR algorithm. The numerical simulation results demonstrate that, when the number of cameras increases, the reconstruction accuracy of the two algorithms increases. The Tikhonov regularization algorithm has a higher precision than the LSQR algorithm. When six cameras are used, the error of reconstructed RMS of the Tikhonov regularization algorithm's temperature and soot volume concentration are 0.0259% and 0.5522%, respectively. On the contrary, those of the LSQR algorithm are 0.3497% and 3.6418%, respectively. Furthermore, the Tikhonov regularization algorithm outperforms the LSQR algorithm in terms of noise immunity. If the LSQR algorithm requires a satisfactory accuracy, the SNR of the flame images should not be less than 65dB. However, for the Tikhonov regularization algorithm, the SNR of the images only need to be better than 39dB, which is much better than that of the LSQR algorithm. Most importantly, the camera separation angle error has a high impact on the reconstruction accuracy. Finally, an angle error of 1° will bring almost 18% error to the Tikhonov regularization algorithm, and more than 100% error to the LSQR algorithm.

Acknowledgments

This research was funded by National Natural Science Foundation of China (NO. 52176144), funded by the Graduate Innovation Program of China University of Mining and Technology (NO. 2022WLKXJ027), funded by Postgraduate Research & Practice Innovation Program of Jiangsu Province (NO. KYCX22_2503).

References

[1] Lee, T.; Bessler, W. G.; Kronemayer, H.; Schulz, C.; Jeffries, J. B., Quantitative temperature measurements in high-pressure flames with multiline NO-LIF thermometry. Applied Optics 2005, 44, (31), 6718-6728.

[2] Chen, H. Y.; Hou, Y. Q.; Wang, X.; Pan, Z. X.; Xu, H. M., Characterization of In-Cylinder Combustion Temperature Based on a Flame-Image Processing Technique. Energies 2019, 12, (12).

[3] Li, W. H.; Lou, C.; Sun, Y. P.; Zhou, H. C., Estimation of radiative properties and temperature distributions in coal-fired boiler furnaces by a portable image processing system. Exp. Therm. Fluid Sci. 2011, 35, (2), 416-421.

[4] Loboda, E. L.; Reino, V. V.; Agafontsev, M. V., CHOICE OF A SPECTRAL RANGE FOR MEASURING TEMPERATURE FIELDS IN A FLAME AND RECORDING HIGH-TEMPERATURE OBJECTS SCREENED BY THE FLAME USING IR DIAGNOSTIC METHODS. Russian Physics Journal 2015, 58, (2), 278-282.

[5] Salinas, C. T.; Pu, Y.; Lou, C.; dos Santos, D. B., Experiments for combustion temperature measurements in a sugarcane bagasse large-scale boiler furnace. Applied Thermal Engineering 2020, 175.

[6] Xiao, X. D.; Choi, C. W.; Puri, I. K., Temperature measurements in steady two-dimensional partially premixed flames using laser interferometric holography. Combustion and Flame 2000, 120, (3), 318-332.

[7] Doi, J.; Sato, S., Three-dimensional modeling of the instantaneous temperature distribution in a turbulent flame using a multidirectional interferometer. Optical Engineering 2007, 46, (1).

[8] Wang, D. Z.; Zhuang, T. G., The measurement of 3-D asymmetric temperature field by using real time laser interferometric tomography. Optics and Lasers in Engineering 2001, 36, (3), 289-297.

[9] Chen, H.; Du, Y.; Ding, Y.; Peng, Z., Non-uniform temperature measurement of flat flames using TDLAS. In Fourth Seminar on Novel Optoelectronic Detection Technology and Application, Guofan, J.; Guangjun, Z., Eds. 2018; Vol. 10697.

[10] Cui, H.; Wang, F.; Huang, Q.; Yan, J.; Cen, K., Multiparameter Measurement in Ethylene Diffusion Flame Based on Time-Division Multiplexed Tunable Diode Laser Absorption Spectroscopy. Ieee Photonics Journal 2019, 11, (3).

[11] Wang, Z.; Zhou, W.; Kamimoto, T.; Deguchi, Y.; Yan, J.; Yao, S.; Girase, K.; Jeon, M.-G.; Kidoguchi, Y.; Nada, Y., Two-Dimensional Temperature Measurement in a High-Temperature and High-Pressure Combustor Using Computed Tomography Tunable Diode Laser Absorption Spectroscopy (CT-TDLAS) with a Wide-Scanning Laser at 1335-1375 nm. Applied Spectroscopy 2020, 74, (2), 210-222.

[12] Most, D.; Leipertz, A., Simultaneous two-dimensional flow velocity and gas temperature measurements by use of a combined particle image velocimetry and filtered Rayleigh scattering technique. Applied Optics 2001, 40, (30), 5379-5387.

[13] Hoffman, D.; Munch, K. U.; Leipertz, A., Two-dimensional temperature determination in sooting flames by filtered Rayleigh scattering. Optics letters 1996, 21, (7), 525-7.

[14] Feng, D.; Goldberg, B. M.; Shneider, M. N.; Miles, R. B., Optimization of Filtered Rayleigh Scattering for the Measurement of Pressure and Temperature. Combustion Science and Technology.

[15] Bookey, H. T.; Bishop, A. I.; Barker, P. F., Narrow-band coherent Rayleigh scattering in a flame. Optics express 2006, 14, (8), 3461-3466.

[16] Kampmann, S.; Leipertz, A.; Dobbeling, K.; Haumann, J.; Sattelmayer, T., Two-dimensional temperature measurements in a technical combustor with laser Rayleigh scattering. Applied optics 1993, 32, (30), 6167-72.

[17] Ma, L.; Li, X.; Sanders, S. T.; Caswell, A. W.; Roy, S.; Plemmons, D. H.; Gord, J. R., 50-kHz-rate 2D imaging of temperature and H2O concentration at the exhaust plane of a J85 engine using hyperspectral tomography. Optics express 2013, 21, (1), 1152-62.

[18] Liu, C.; Cao, Z.; Lin, Y.; Xu, L.; McCann, H., Online Cross-Sectional Monitoring of a Swirling Flame Using TDLAS Tomography. Ieee Transactions on Instrumentation and Measurement 2018, 67, (6), 1338-1348.

[19] Liu, X. D.; Hao, X. J.; Xue, B.; Tai, B.; Zhou, H. C., Two-Dimensional Flame Temperature and Emissivity Distribution Measurement Based on Element Doping and Energy Spectrum Analysis. Ieee Access 2020, 8, 200863-200874.

[20] Zapka, W.; Pokrowsky, P.; Tam, A. C., Noncontact optoacoustic monitoring of flame temperature profiles. Optics letters 1982, 7, (10), 477-9.

[21] Liu, D.; Yan, J. H.; Wang, F.; Huang, Q. X.; Chi, Y.; Cen, K. F., Simultaneous experimental reconstruction of three-dimensional flame soot temperature and volume fraction distributions. Acta Physica Sinica 2011, 60, (6).

[22] Liu, G. N.; Liu, D., Inverse radiation analysis for simultaneous reconstruction of temperature and volume fraction fields of soot and metal-oxide nanoparticles in a nanofluid fuel sooting flame. International Journal of Heat and Mass Transfer 2018, 118, 1080-1089.

[23] Liu, D.; Huang, Q. X.; Wang, F.; Chi, Y.; Cen, K. F.; Yan, J. H., Simultaneous Measurement of Three-Dimensional Soot Temperature and Volume Fraction Fields in Axisymmetric or Asymmetric Small Unconfined Flames With CCD Cameras. Journal of Heat Transfer-Transactions of the Asme 2010, 132, (6).

[24] Jiang, F.; Liu, S.; Liangi, S. Q.; Li, Z. H.; Wang, X. Y.; Lu, G., Visual Flame Monitoring System Based on Two-Color Method. Journal of Thermal Science 2009, 18, (3), 284-288.

[25] Li, Z. H.; Liu, S.; Mu, H. P.; Jiang, F.; Guo, J. M., Calibration and Experimental Research of a Multiple-wavelength Flame Temperature Instrumentation System. Journal of Thermal Science 2004, 13, (4), 371-375.

[26] Huang, Y.; Yan, Y., Transient two-dimensional temperature measurement of open flames by dual-spectral image analysis. Trans. Inst. Meas. Control 2000, 22, (5), 371-384.

[27] Huang, Q. X.; Liu, D.; Wang, F.; Yan, J. H.; Chi, Y.; Cen, K. F., Study on three-dimensional flame temperature distribution reconstruction based on truncated singular value decomposition. Acta Physica Sinica 2007, 56, (11), 6742-6748.

[28] Liu, D.; Wang, F.; Cen, K. F.; Yan, J. H.; Huang, Q. X.; Chi, Y., Noncontact temperature measurement by means of CCD cameras in a participating medium. Optics Letters 2008, 33, (5), 422-424.

[29] Liu, L. H.; Tan, H. P., Inverse radiation problem in three-dimensional complicated geometric systems with opaque boundaries. Journal of Quantitative Spectroscopy & Radiative Transfer 2001, 68, (5), 559-573.

[30] Liu, D.; Wang, F.; Yan, J. H.; Huang, Q. X.; Chi, Y.; Cen, K. F., Inverse radiation problem of temperature field in three-dimensional rectangular enclosure containing inhomogeneous, anisotropically scattering media. International Journal of Heat and Mass Transfer 2008, 51, (13-14), 3434-3441.

[31] Rukolaine, S. A., Regularization of inverse boundary design radiative heat transfer problems. Journal of Quantitative Spectroscopy & Radiative Transfer 2007, 104, (1), 171-195.

[32] Daun, K. J.; Howell, J. R., Inverse design methods for radiative transfer systems. Journal of Quantitative Spectroscopy and Radiative Transfer 2005, 93, (1), 43-60.

[33] Qiu, S. R.; Lou, C.; Xu, D. D., A HYBRID METHOD FOR RECONSTRUCTING TEMPERATURE DISTRIBUTIONS IN A RADIANT ENCLOSURE. Numerical Heat Transfer Part a-Applications 2014, 66, (10), 1097-1111.

[34] Zhou, H.-C.; Han, S.-D.; Sheng, F.; Zheng, C.-G., Visualization of three-dimensional temperature distributions in a large-scale furnace via regularized reconstruction from radiative energy images: numerical studies %J Journal of Quantitative Spectroscopy and Radiative Transfer. 2002, 72, (4).

[35] Lou, C.; Zhou, H.-C., ASSESSMENT OF REGULARIZED RECONSTRUCTION OF THREE-DIMENSIONAL TEMPERATURE DISTRIBUTIONS IN LARGE-SCALE FURNACES. Numerical Heat Transfer Part B-Fundamentals 2008, 53, (6), 555-567.

[36] Daun, K. J.; Thomson, K. A.; Liu, F.; Smallwood, G. J., Deconvolution of axisymmetric flame properties using Tikhonov regularization. Applied Optics 2006, 45, (19), 4638-4646.

[37] Zhou, H.-C.; Lou, C.; Cheng, Q.; Jiang, Z.; He, J.; Huang, B.; Pei, Z.; Lu, C., Experimental investigations on visualization of three-dimensional temperature distributions in a large-scale pulverized-coal-fired boiler furnace %J Proceedings of the Combustion Institute. 2004, 30, (1).

[38] Wei, C.; Schwarm, K. K.; Pineda, D. I.; Spearrin, R. M., Volumetric laser absorption imaging of temperature, CO and CO2 in laminar flames using 3D masked Tikhonov regularization. Combustion and Flame 2021, 224, 239-247.

[39] Xie, Z. C.; Wang, F.; Yan, J. H.; Cen, K. F., Comparative studies of Tikhonov regularization and truncated singular value decomposition in the three-dimensional flame temperature field reconstruction. Acta Physica Sinica 2015, 64, (24).

[40] Huang, Q. X.; Wang, F.; Liu, D.; Ma, Z. Y.; Yan, J. H.; Chi, Y.; Cen, K. F., Reconstruction of soot temperature and volume fraction profiles of an asymmetric flame using stereoscopic tomography. Combustion and Flame 2009, 156, (3), 565-573.

[41] Wang, F.; Yan, J. H.; Cen, K. F.; Huang, Q. X.; Liu, D.; Chi, Y.; Ni, M. J., Simultaneous measurements of two-dimensional temperature and particle concentration distribution from the image of the pulverized-coal flame. Fuel 2010, 89, (1), 202-211.

[42] Lou, C.; Zhou, H.-C., Decoupled reconstruction method for simultaneous estimation of temperatures and radiative properties in a one-dimensional, gray, participating medium. Numerical Heat Transfer Part B-Fundamentals 2007, 51, (3), 275-292.

[43] Lou, C.; Zhou, H.-C.; Yu, P.-F.; Jiang, Z.-W., Measurements of the flame emissivity and radiative properties of particulate medium in pulverized-coal-fired boiler furnaces by image processing of visible radiation. Proceedings of the Combustion Institute 2007, 31, 2771-2778.

[44] Lou, C.; Li, W. H.; Zhou, H. C.; Salinas, C. T., Experimental investigation on simultaneous measurement of temperature distributions and radiative properties in an oil-fired tunnel furnace by radiation analysis. International Journal of Heat and Mass Transfer 2011, 54, (1-3), 1-8.

[45] Yan, W. J.; Lou, C., Two-dimensional distributions of temperature and soot volume fraction inversed from visible flame images. Exp. Therm. Fluid Sci. 2013, 50, 229-233.

[46] Ufuah, E.; Bailey, C. G. In Flame Radiation Characteristics of Open Hydrocarbon Pool Fires, World Congress on Engineering (WCE 2011), Imperial Coll, London, UNITED KINGDOM, Jul 06-08, 2011; Imperial Coll, London, UNITED KINGDOM, 2011; pp 1952-1958.

[47] Charalampopoulos, T. T.; Chang, H. J. C. S.; Technology, In Situ Optical Properties of Soot Particles in the Wavelength Range from 340 nm to 600 nm. 1988, 59, (4-6), 401-421.

[48] Regińska, T., A Regularization Parameter in Discrete Ill-Posed Problems. 1996, 17, (3), 740-749.